Journal of Materials Chemistry C

ROYAL SOCIETY OF CHEMISTRY

PAPER

View Article Online
View Journal | View Issue

Cite this: J. Mater. Chem. C, 2023, 11, 7389

$[W_{10}O_{32}]^{4-}$-based POMOFs with different nuclear cobalt clusters for photoreduction of CO_2 to produce syngas†

Si-Qi You,‡[a] Yu-Jiao Dong,‡[a] Bao-Shan Hou,[a] Man Dong,[a] Jia-Lin Tong,[a] Ling-Xin Wang,[b] Xin-Long Wang,*[a] Chun-Yi Sun,*[a] Wei Guan*[a] and Zhong-Min Su[ab]

Received 3rd March 2023,
Accepted 10th May 2023

DOI: 10.1039/d3tc00775h

rsc.li/materials-c

The CO_2 emissions from flue gases in traditional electricity generation and industrial sectors account for the main source of global emissions. The direct conversion of CO_2 in flue gases into value-added carbon production is a low-cost and simple process to realize a carbon neutral cycle, yet the development of an efficient catalyst to treat the CO_2 in flue gases is still in its infancy. Here, we present two polyoxometalate-based metal organic frameworks (POMOFs) with $[W_{10}O_{32}]^{4-}$ as the connecting node, named $Co_2(W_{10}O_{32})(BIA)_4(CH_3CN)_4$ (compound **1**) and $Co_4(W_{10}O_{32})(INA)_6(CH_3CN)_4(TBA)_2$ (compound **2**), as catalysts for the photoreduction of CO_2 in exhaust gases. Under a pure CO_2 atmosphere, syngas is the main product and the yield of compound **1** is 72.7 μmol h^{-1}, which is ~40% higher than that of compound **2** (54.2 μmol h^{-1}). Notably, the yield of compound **1** reaches 42.7 μmol h^{-1} with 15% CO_2 in the flue gas, which indicates that the catalyst can not only overcome the low CO_2 concentration but also tolerate the harsh gas composition in the flue gas. In addition, density functional theory (DFT) calculations show that the charge distribution and steric hindrance of compound **1** were conducive to the reduction reaction.

Introduction

In recent years, rapid urbanisation and industrialisation have led to an increasing trend of CO_2 emissions.[1] The increasing concentration of CO_2 in the environment is an important factor affecting global climate change.[2–4] Photocatalytic CO_2 reduction technology driven by solar energy is considered as one of the favourable ways to address CO_2 due to its clean energy and mild reaction conditions.[5,6] Currently, photocatalysts are mostly used to obtain high purity CO_2. However, CO_2 in the flue gases of the electricity generation and industrial sectors accounts for the majority of global CO_2 emissions. The concentration of CO_2 in the flue gas is relatively low.[7,8] Therefore, direct conversion of CO_2 from flue gas to carbonaceous fuels or other value-added products using photocatalysts is an inexpensive and simple way to achieve the carbon cycle.[9] At present, the development of low concentration CO_2 photocatalysts in flue gas is in the initial stages and the application of CO_2 photocatalysts for flue gas applications is imminent. Such catalysts must not only overcome the limitation of CO_2 concentration, but also tolerate the remaining components in the flue gas.[10] Therefore, the development of photocatalysts for direct application of CO_2 in flue gas is a great challenge.

Polyoxometalate-based metal organic frameworks (POMOFs) are extended architectures that introduce polyoxometalate (POMs) units into metal organic frameworks (MOFs), which contain two types of integration, either using the cavities present in the MOF structure to encapsulate the POMs or using the POMs as a building block in the MOF structure.[11] The POMs are a class of inorganic metal cluster bridged by oxygen atoms with structural adjustability, composition diversity and efficient electron transfer storage ability.[12–19] The MOFs are crystalline materials with intramolecular pores formed by the self-assembly of organic ligands and metal nodes using coordination bonds with an excellent light absorption ability, abundant porosity and internal tunability.[20–27] Combining the advantages of POMs and MOFs, POMOFs are widely used in battery,[28] detection,[29] photochromism,[30] and photoelectric catalysis applications.[31–34] Despite the advantages of POMOFs, their application in the field of CO_2 photoreduction is still in its infancy,[35–37] let alone photoreduction of

[a] Key Laboratory of Polyoxometalate Science of Ministry of Education, Northeast Normal University, Changchun, Jilin 130024, People's Republic of China
[b] Jilin Provincial Science and Technology Innovation Center of Optical Materials and Chemistry, School of Chemistry and Environmental Engineering, Changchun University of Science and Technology Changchun, Jilin 130022, China

† Electronic supplementary information (ESI) available. CCDC 2245817 and 2245818. For ESI and crystallographic data in CIF or other electronic format see DOI: https://doi.org/10.1039/d3tc00775h

‡ These authors contributed equally to this work.

CO_2 in low CO_2 concentration or even direct use of industrial waste gas.

Here, we present two new POMOFs based on ($[W_{10}O_{32}]^{4-}$) named as $Co_2(W_{10}O_{32})(BIA)_4(CH_3CN)_4$ (compound **1**) and $Co_4(W_{10}O_{32})(INA)_6(CH_3CN)_4(TBA)_2$ (compound **2**). The syngas yield of compound **1** with a mononuclear cobalt cluster is 72.7 μmol h^{-1}, which is higher than that of compound **2** with a binuclear cobalt cluster (54.2 μmol h^{-1}). compound **1** retained its high reactivity in dilute CO_2 (5–30%). In particular, the syngas yield in 30% CO_2 is 53.3 μmol h^{-1}, which is 75% of the pure CO_2 yield. Furthermore, the syngas yield of compound **1** in the simulated industrial flue gas system is 42 μmol h^{-1}, which indicates that the catalyst is resistant to poisoning from the exhaust gases. This work provides a promising photocatalyst for the preparation of syngas at a low CO_2 concentration and under flue gas conditions.

Experimental section

Synthesis of $(TBA)_4[W_{10}O_{32}]$

The $(TBA)_4[W_{10}O_{32}]$ was synthesised according to a method published in the literature and with slight modifications.[38,39] Tetrabutylammonium bromide (TBAB) (0.97 g, 3 mmol) and deionised water (300 mL) were added to a 1 L beaker. The $Na_2WO_4{\cdot}2H_2O$ (2 g, 6 mmol) and deionised water (300 mL) were added to another 1 L beaker. The two solutions were stirred and heated to 90 °C. Concentrated hydrochloric acid was added to both solutions until the pHs were both 2. After acidification, the solutions from the two beakers were mixed and the stirring was continued at 90 °C until all the dissolved white solids were precipitated. After the reaction, the solution was cooled to room temperature and subsequently filtered to obtain a white solid sample. The solid was washed 2–3 times with water and ethanol, and then dried at 60 °C under vacuum. The dried sample was dissolved in 10 mL of hot acetonitrile (CH_3CN) and then placed in a freezer at −20 °C for 12 h. After filtration, the filtrate was collected and then evaporated to obtain the product as a white solid.

Synthesis of $Co_2(W_{10}O_{32})(BIA)_4(CH_3CN)_4$ (compound 1)

The $(TBA)_4[W_{10}O_{32}]$ (0.01 mmol, 33 mg), $CoCl_2{\cdot}6H_2O$ (0.1 mmol, 23.8 mg), 1*H*-benzimidazole-5-carboxylic acid (BIA, 0.1 mmol, 20 mg) and CH_3CN (5 mL) were added to a Teflon lined autoclave (15 mL). The solvent mixture was stirred for 30 min at room temperature and then kept at 75 °C for 24 h. The autoclave was cooled to room temperature and brown-black crystals appeared (47% yield based on Co).

Synthesis of $Co_4(W_{10}O_{32})(INA)_6(CH_3CN)_4(TBA)_2$ (compound 2)

The $(TBA)_4[W_{10}O_{32}]$ (0.01 mmol, 33 mg), $Co(NO_3)_2{\cdot}6H_2O$ (0.1 mmol, 29.1 mg), isonicotinic acid (INA) (0.1 mmol, 13 mg) and CH_3CN (5 mL) were added to a Teflon lined autoclave (15 mL). The solvent mixture was stirred for 30 min at room temperature and then kept at 85 °C for 24 h. The autoclave was then cooled to room temperature and purple crystals appeared (61% yield based on Co).

Results and discussion

Catalyst characterisation

Single-crystal X-ray diffraction data (XRD) showed that compound **1** crystallises in the triclinic space group $P\bar{1}$ (Table S1, ESI†). The asymmetric unit of compound **1** contained two Co^{2+}, two CH_3CN molecules, two BIA ligands and 1/2 $[W_{10}O_{32}]^{4-}$. Both Co^{2+} in compound **1** adopted a coordination number of six and exhibited an octahedral geometry. The Co1 coordinated with two nitrogen atoms from the BIA ligands, two nitrogen atoms from the CH_3CN molecules and two oxygen atoms from $[W_{10}O_{32}]^{4-}$ to form a twisted octahedron. The coordination geometry of Co2 was similar to that of Co1, with the difference that two oxygen atoms provided by $[W_{10}O_{32}]^{4-}$ were in different positions. The Co–O bond length ranged from 2.07 (3) −2.09 (3) Å and the range of the Co–N bond lengths were 2.086 (19) −2.17 (4) Å. Each Co^{2+} was linked to two adjacent $[W_{10}O_{32}]^{4-}$, two BIA ligands and two CH_3CN molecules to form a mononuclear cobalt cluster (Fig. 1a). Each $[W_{10}O_{32}]^{4-}$ was connected to four mononuclear cobalt clusters *via* oxygen atoms (Fig. 1b). For ease of description, the $[W_{10}O_{32}]^{4-}$ and mononuclear cobalt clusters are simplified as a 4-connected node and a 2 connected node, respectively. $[W_{10}O_{32}]^{4-}$ and the mononuclear cobalt clusters interconnect to form a topological structure (Fig. 1c).

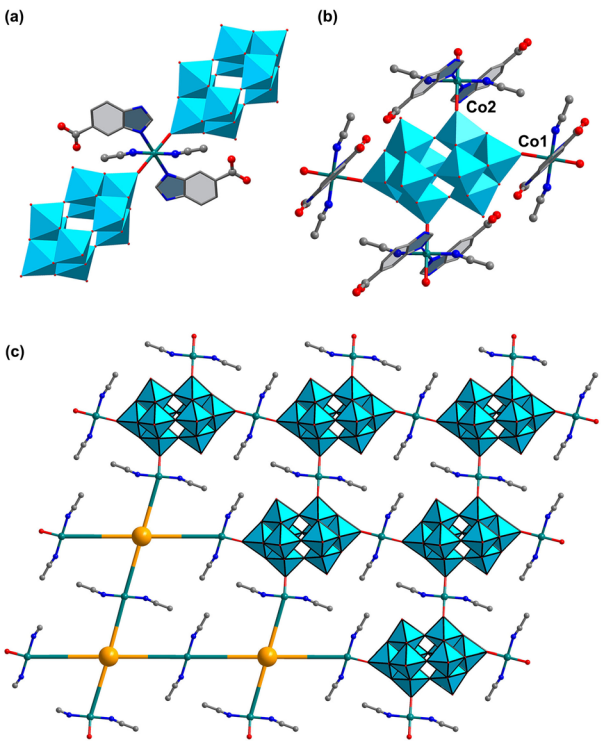

Fig. 1 (a) The coordination environment of the mononuclear cobalt cluster in compound **1**. (b) The coordination environment of $[W_{10}O_{32}]^{4-}$ in compound **1** (green balls: Co, red balls: O, blue balls: N, grey balls: C, blue polyhedron: $[W_{10}O_{32}]^{4-}$). (c) Mononuclear cobalt clusters are simplified as dark green connected nodes, and $[W_{10}O_{32}]^{4-}$ was simplified as orange connected nodes. The dark green and orange connected nodes were connected to form a topological structure.

Compound **2** crystallised in the monoclinic $P2_1/n$ space group (Table S2, ESI†). The asymmetric unit of Compound **2** contained two Co^{2+}, two CH_3CN molecules, three INA ligands and one half of the $[W_{10}O_{32}]^{4-}$ polyanion. Based on the charge balance, the unit should contain one disordered tetrabutylammonium (TBA). This was a by-product from the decomposition of $(TBA)_4[W_{10}O_{32}]$)[40] Both the Co^{2+} ions in compound **2** adopted a coordination number of six with an octahedral configuration. The Co1 coordinated with one nitrogen atom from an INA ligand, four oxygen atoms from INA ligands and one oxygen atom from $[W_{10}O_{32}]^{4-}$. The Co2 atoms connected with one nitrogen atom from an INA ligand, three oxygen atoms from an INA ligand and two nitrogen atoms from a CN_3CN molecule. The Co–O and Co–N bond lengths ranged from 2.008 (8) −2.246 (8) Å and 2.089 (8) −2.163 (12) Å, respectively. Three INA acted as bridging ligands to link Co1 and Co2 into a binuclear Co cluster with a distance of 3.5168 (21) Å between Co–Co. As shown in Fig. 2a, two oxygen atoms provided by a $[W_{10}O_{32}]^{4-}$ connected two binuclear Co clusters. Each binuclear Co cluster connected one $[W_{10}O_{32}]^{4-}$ and four adjacent binuclear Co clusters (Fig. 2b). The binuclear cobalt cluster and $[W_{10}O_{32}]^{4-}$ were connected to each other to form a 3D POMOF structure (Fig. 2c). Compound **2** can be viewed as a 3D column-supported pillared structure. The binuclear Co clusters are bridged by INA ligands to form 2D grids (as shown in the Fig. 2d), and adjacent 2D grids are bridged by $[W_{10}O_{32}]^{4-}$ as column support agents to form a 3D column support structure, which has the advantage of structural tunability and stability.

The crystallinity and phase purity of compounds **1** (Fig. 3a) and **2** (Fig. 3b) were characterised by XRD. The experimental patterns of compound **1** and **2** were in good agreement with the simulated data, and showed the phase purification in compound **1** and **2**. The compositional structures of compound **1** (Fig. 3c) and compound **2** (Fig. 3d) were characterised by Fourier transform infrared (FT-IR) analysis. The IR spectra of both *vs.* showed the characteristic vibrations of the $[W_{10}O_{32}]^{4-}$. The spectral bands at 959 cm^{-1} in Fig. 3c and 955 cm^{-1} in Fig. 3d were attributed to W = O_t. The two peaks observed at 898 cm^{-1} in Fig. 3c and at 894 cm^{-1} in Fig. 3d originates from W–O–W. In addition, the peaks at 797 cm^{-1} in Fig. 3c and at 794 cm^{-1} in Fig. 3d were associated with W–O_e–W.[41,42] The optical absorption and electronic structures of compounds **1** and **2** were studied by UV-Vis diffuse reflectance spectroscopy. As shown in Fig. 3e and f, both compounds had two sets of absorption bands. The strong absorption bands located at approximately 310 nm in Fig. 3e and at 340 nm in Fig. 3f can be attributed to the charge transfer from the oxygen atom to the tungsten atom in $[W_{10}O_{32}]^{4-}$.[43] In addition, the broad absorption bands from 500 to 700 nm in compound **1** (Fig. 3e) and from 430 to 700 nm in compound **2** (Fig. 3f) may originate from the 3d–4d electronic transitions of Co^{2+}.[44,45] The absorption spectra of the two POMOFs with $[W_{10}O_{32}]^{4-}$ as the connecting node showed partial overlap with the solar emission spectrum. This provides the possibility for use in a subsequent application of photocatalysis.[46] The energy band gaps of compound **1** and compound **2** were calculated to be 2.73 (Fig. 3e, insert) and 2.91 eV (Fig. 3f, insert), respectively, using the Tauc plot equation.

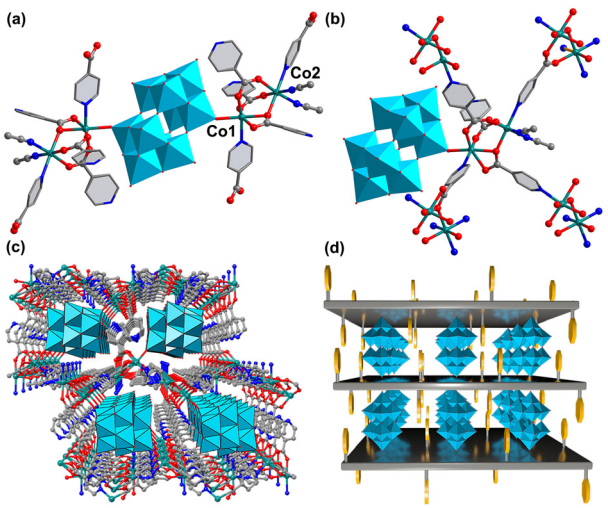

Fig. 2 (a) The coordination environment of $[W_{10}O_{32}]^{4-}$ in compound **2**. (b) The coordination environment of a binuclear Co cluster in compound **1** (green balls: Co, red balls: O, blue balls: N, and grey balls: C, blue polyhedron: $[W_{10}O_{32}]^{4-}$). (c) A 3D view of compound **2**. (d) Schematic diagram of the pillared structure of compound **2**.

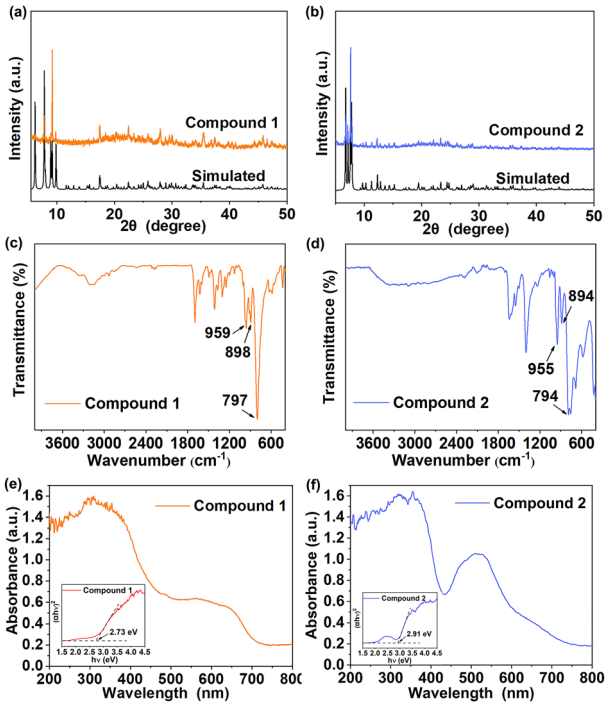

Fig. 3 (a) and (b) Experimental and simulated PXRD patterns of compound **1** and **2**. (c) and (d) Fourier transform infrared spectroscopy (FT-IR) of compound **1** and **2**. (e) the UV-Vis diffuse reflectance spectroscopy of compound **1**, and Tauc plot of compound **1** for band gap calculation based on the UV-vis diffusion spectrum (insert); (f) UV-Vis diffuse reflectance spectroscopy of compound **2**, and a Tauc plot of compound **2** for band gap calculation based on the UV-vis diffusion spectrum (insert).

Photocatalytic performance tests

Photocatalytic experiments were performed in 6 mL of a mixed solution (water/CH_3CN/TEOA; v/v/v = 1 : 4 : 1). $[Ru(bpy)_3]Cl_2$

(7.5 mg, 0.01 mmol) was added to the solution as a photosensitiser and pure CO_2 was utilised as the reaction condition. To determine the optimal input mass of the system, different masses of catalyst were input into the system with $[Ru(bpy)_3]Cl_2$ (7.5 mg, 0.01 mmol) as a fixed value. As shown in Fig. 4a, the syngas yield increased from 61 μmol h^{-1} to 72.7 μmol h^{-1} when the mass of compound **1** was increased from 0.5 to 1 mg (Fig. 4a). However, a further increase in the mass of compound **1** caused a decrease in the catalytic activity. The yield of compound **1** (2 mg) was 59.3 μmol h^{-1} and there was a yield of 43.5 μmol h^{-1} with a mass increase to 3 mg. A similar yield trend appeared in the catalytic system of compound **2**. The previous trend may be due to the fact that the increase of the photocatalyst in the system will hinder the number of photons absorbed per unit of photosensitiser, which eventually leads to a decrease in the activity of the catalytic system.[47] Therefore, there is an optimal ratio between the catalyst mass and the photosensitiser in the catalytic system, and the optimal mass ratio of compounds **1** and **2** to $[Ru(bpy)_3]Cl_2$ was 0.13 (1/7.5, *m/m*). Subsequent catalytic experiments were carried out using 1 mg of catalyst as a standard. The time course reaction plots for the catalysts are shown in Fig. 4c and d. The CO and H_2 yields of both catalytic systems showed time-dependent trends. A significant decrease in yield was detected after 45 min for compound **1** and after 30 min for compound **2**. These results may be attributed to the partial deactivation of the photosensitiser.[48] The H_2:CO ratio of compound **1** was found to be approximately 1 and this ratio could be used to produce low carbon hydrocarbons.[49–51] Meanwhile, the quantum efficiency (QE) value was measured for CO at 420 nm over 1 h (0.63% for compound **1**, and 0.59% for compound **2**), which were higher than those of many others reported in the literature (Table S3, ESI†). Cycling experiments were used to explore the catalytic stability of compound **1** and **2**. The two catalysts still maintained a high activity after three rounds of catalytic experiments (Fig. S1a and S1b, ESI†).

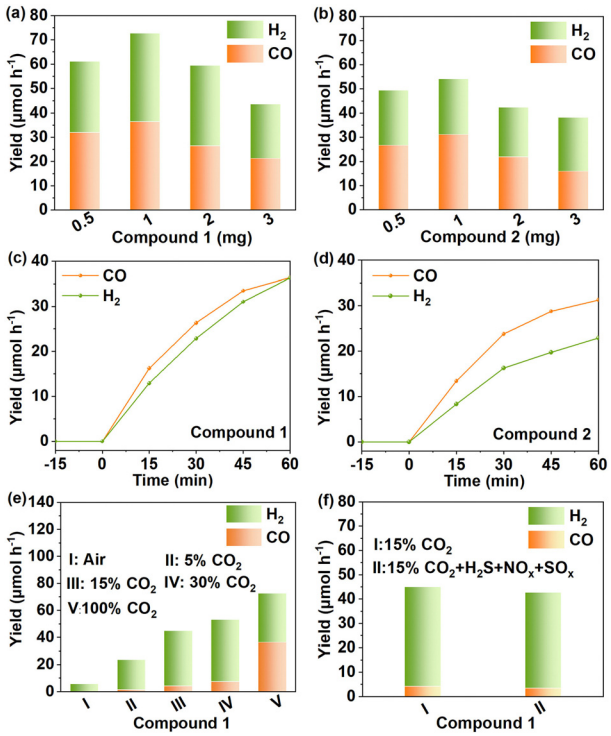

Fig. 4 (a) and (b) Syngas evolution with different quantities of compound **1** and **2**. (c) The time course reaction plots of compound **1** (1 mg). (d) The time course reaction plots of compound **2** (1 mg). (e) the photocatalytic catalytic test plots of compound **1** (1 mg) under different concentrations of CO_2: I was air conditions (containing 0.03% CO_2) and II–V were different concentrations of CO_2/Ar gas. (f) Photocatalytic control chart of compound **1** (1 mg) under 15% CO_2/Ar gas and 15% CO_2 simulated flue gas conditions with 0.2% H_2S, 0.2% NO_x and 0.2% SO_x in a 15% CO_2/N_2 system.

Subsequently, the catalytic activity of POMOF was investigated at low CO_2 concentrations using compound **1** as a catalyst. The CO_2 concentrations were set to 0.03% (air conditions), 5%, 15% and 30%. As shown in Fig. 4e, the syngas yield of 30% CO_2 reached 53.3 μmol h^{-1}, which was 75% of the syngas yield under pure CO_2 conditions. Even at lower CO_2 concentration conditions, compound **1** still maintained a high activity, with syngas yields of 5.9, 23.6 and 45 μmol h^{-1} for 0.03%, 5% and 15% CO_2 concentration conditions, respectively. These results indicate that the syngas yield was not completely affected by the CO_2 concentration, which leads to the possibility of a low CO_2 concentration reduction.

In order to verify the activity of compound **1** under flue gas conditions, the composition of the flue gas was simulated,[52] and this including CO_2 (15%), H_2S (0.2%), SO_x (0.2%), NO_x (0.2%) and N_2. As shown in Fig. 4f, the yield of the syngas under flue gas conditions was 42.7 μmol h^{-1}, which was close to the 15% CO_2 yield. This result indicates that compound **1** is tolerant to other components in the exhaust gases.

Controlled experimental tests were performed to verify the necessity of each component. The product was barely detectable in the absence of $[Ru(bpy)_3]Cl_2$, indicating that the reduction process may require photosensitisation by a photosensitiser (Fig. S2(II), ESI†). The composition of the reaction medium also affected the catalytic effect. Almost no reaction occurred in the photocatalytic system lacking triethanolamine (TEOA), which may be attributed to the fact that TEOA acted as a sacrificial agent for the catalytic system (Fig. S2(III), ESI†). The syngas yield plummeted when the mixed solution changed to TEOA (1 mL) and CH_3CN (5 mL). This suggests that H_2O may be a key donor of hydrogen protons Fig. S2(IV), ESI†).[53] Under dark conditions, almost no gaseous products were detected, suggesting that light was an important energy source (Fig. S2(V), ESI†). No CO production was detected by replacing CO_2 with N_2, which suggested that the carbon-containing products of the system originated from CO_2 (Fig. S2(VI), ESI†). The isotope labelling experiment of compounds **1** and **2** proves that the reduction of CO_2 occurred in the system (Fig. S3a and S3b, ESI†).

Possible photocatalytic mechanism

In order to reveal the photoreaction process of compounds **1** and **2**, *in situ* IR tests were performed on both of the catalysts to determine the reaction intermediates. The experimental data were collected for analysis at different times. The peaks belonging to compound **1** at 1132 cm^{-1} (Fig. 5a) and to compound **2** at

1135 cm^{-1} (Fig. 5b) were attributed to H_2CO, and the peaks at 1338 cm^{-1} (Fig. 5a) and 1326 cm^{-1} (Fig. 5b) were ascribed to m-CO_3^{2-}. The characteristic peaks observed at 1518 cm^{-1} (Fig. 5a) and 1529 cm^{-1} (Fig. 5b) belonged to COOH*, which was a key intermediate in the conversion of CO_2 to CO. The intensity of the COOH* peaks attributed to compounds **1** and **2** gradually increased with the extension of the time of light irradiation, indicating that CO_2 was continuously converted to CO.[54–59]

The energy level structure and the charge transfer mechanism of compounds **1** and **2** were inferred from the Mott–Schottky plots (Fig. 5c and d). The flat-band potential of compound **1** was tested at frequencies of 1200, 1500 and 2000 Hz as −0.92 V *vs.* Ag/AgCl. The Mott–Schottky plot showed that the slope of the tangent line of compound **1** was positive, indicating that compound **1** was an N-type semiconductor. For the N-type semiconductor, the bottom of the conduction band (CB) is about 0.1 V negative to the flat band potential,[60] so the CB of compound **1** was −0.82 V *vs.* NHE. The flat band potential of compound **2** was −0.85 V *vs.* Ag/AgCl (−0.65 V *vs.* NHE) and the CB was −0.75 V *vs.* NHE. According to the equation: $E_{CB} = E_{VB} - E_g$, the valence bands (VB) of compounds **1** and **2** were found to be 1.91 V and 2.16 V *vs.* NHE, respectively. The energy level structures of compound **1** and **2** indicated that both could be used for syngas generation (CO_2/CO = −0.53 *vs.* NHE; H^+/H_2 = −0.42 *vs.* NHE).[61] One of the reasons for the difference in catalytic effect may be that there was a larger energy level difference between compound **1** and the reduction products, which may be more conducive to the occurrence of a reduction reaction.[62]

The electronic orbital distribution of compounds **1** and **2** was determined by DFT calculations. As shown in Fig. 6a and b, the lowest unoccupied molecular orbitals (LUMO) of compounds **1** and **2** were mainly distributed on the cobalt ion directly connected to $[W_{10}O_{32}]^{4-}$ (Co1). This type of cobalt ion can be an active centre and would easily accept electrons from the photosensitiser. To investigate the reason for the difference in catalytic effect of compounds **1** and **2**, we combined the interaction region indicator (IRI) in the Multiwfn software to visually exhibit the interaction regions corresponding to covalent bonds and weak interactions. Fig. 6c and d shows that the red region around Co1 in compound **1** circled in yellow is significantly smaller that around Co1 in compound **2**, indicating that the notable repulsion of Co1 in compound **1** was weaker than that in compound **2**. Therefore, the active center Co1 in compound **1** may facilitate the initiation of the reduction reaction.[63,64]

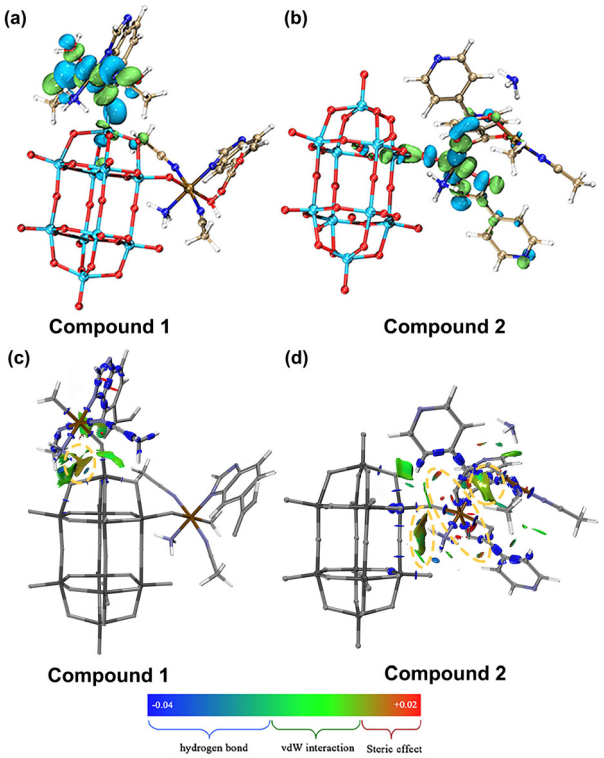

Fig. 6 (a) and (b) Schematic diagrams of the LUMO orbital of compounds **1** and **2**, (c) and (d) the IRI analysis (IRI = 0.8) of compounds **1** and **2**; blue represents attraction, green represents a weak interaction, and red represents a steric effect.

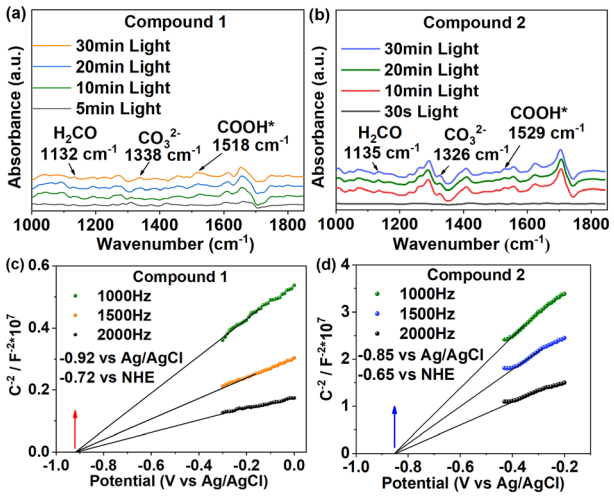

Fig. 5 (a) and (b) *In situ* IR tests of compounds **1** and **2** were performed using a 300 W xenon lamp with an AM1.5 filter as the light source. (c) and (d) The Mott–Schottky plots for compound **1** and **2** at frequencies of 1000, 1500 and 2000 Hz.

To investigate the quenching mechanism of the CO_2 photoreduction. The catalyst and TEOA were placed into the CH_3CN solution of $[Ru(bpy)_3]Cl_2$ to investigate the fluorescence emission spectra. As shown in Fig. 7a and b, the CH_3CN solution of $[Ru(bpy)_3]Cl_2$ exhibited an emission band centred at 620 nm at an excitation wavelength of 382 nm. The fluorescence intensity gradually grew weaker when different masses of compound **1** or **2** were used. However, the fluorescence intensity did not change significantly with the addition of different volumes of TEOA (Fig. 7c). These results suggest that the excited electrons of $[Ru(bpy)_3]Cl_2$ were transferred to the catalysts rather than to the TEOA.[65] To further elucidate the electron transfer behaviour of compounds **1** and **2** during the reaction, cyclic voltammetry (CV) was conducted on compounds **1** and **2**.[66,67] The CV curves obtained showed that compounds **1** and **2** presented reduction waves at −0.88 (Fig. S4a, ESI†) and −0.83 V *vs.* Ag/AgCl (Fig. S4b, ESI†), which were generally considered to be

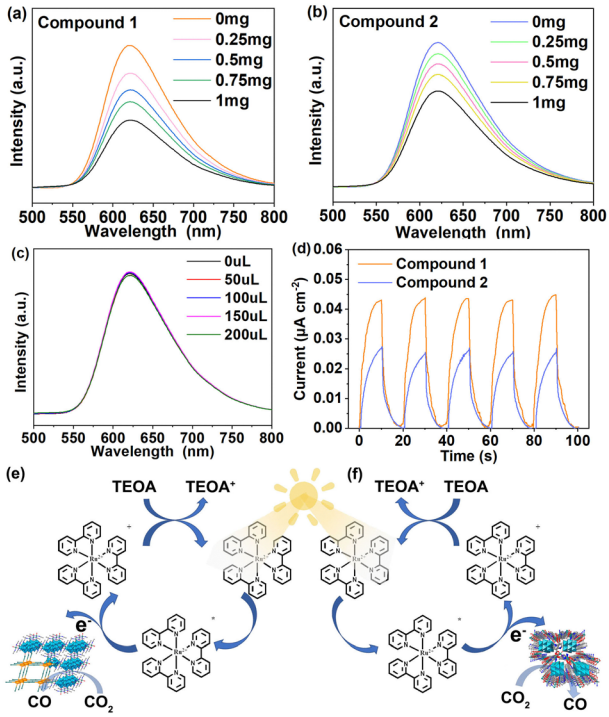

Fig. 7 (a) and (b) The fluorescence emission spectra of compounds **1** and **2** added to CH_3CN solutions with different masses of $[Ru(bpy)_3]Cl_2$. (c) The fluorescence emission spectra of different volumes of TEOA added to CH_3CN solutions of $[Ru(bpy)_3]Cl_2$. (d) Photocurrent responses of compounds **1** and **2**. (e) and (f) Schematic diagrams of the mechanism of photocatalytic reduction of CO_2 by compounds **1** and **2**.

Co^{II}/Co^{I}.[68–70] The LUMO of compounds **1** and **2** were mainly distributed on cobalt ions, and was analysed used DFT calculations. The process of electron transfer may be that the excited photoelectrons from $[Ru(bpy)_3]Cl_2$ transferred to the Co site by the internal transfer of the catalyst, and further reduced the Co^{2+} to Co^{+}.[71] In this process the CO_2 and H^+ were reduced to produce CO and H_2 at the metal cobalt active sites.[72] The charge separation of compounds **1** and **2** was investigated using a photocurrent test. As shown in Fig. 7d, the photocurrent value rose rapidly under light conditions and fell rapidly when the light was turned off, indicating that both materials responded well to light. The highest current value of compound **1** was about 0.043 μA cm^{-2} and this could be cycled stably for five rounds. The highest current value of compound **2** was about 60% lower than that of compound **1** (0.027 μA cm^{-2}). The higher photocurrent value of compound **1** indicated the better charge separation of the material. This may make compound **1** more effective in catalysis compared to compound **2**.

Based on the previous experimental results, a possible reaction mechanism of the catalytic system is proposed. The LUMO and the highest occupied molecular orbital (HOMO) of $[Ru(bpy)_3]Cl_2$ were −1.25 and 1.24 V *vs.* NHE, respectively. The $[Ru(bpy)_3]Cl_2$ was illuminated to produce an excited state with the potential of −1.09 V *vs.* NHE ($E(Ru(bpy)_3^{2+*}/Ru(bpy)^{3+})$).[72,73] The CBM of compounds **1** and **2** were obtained from the Mott–Schottky plots as −0.82 and −0.75 V *vs.* NHE, respectively. Therefore, both catalysts had suitable potentials to accept electrons to effect the CO_2 and H^+ reduction. From the DFT calculations, it was found that the active centres of compounds **1** and **2** were mainly distributed on cobalt ions.[74,75] The electron transfer process may be that $[Ru(bpy)_3]Cl_2$ was excited by light irradiation to generate $Ru(bpy)_3^{2+*}$, followed by the $Ru(bpy)_3^{2+*}$ being quenched to form $Ru(bpy)_3^{3+}$ by the electron transfer to the catalysts, and Co^{2+} was reduced to Co^{+} by the internal transfer of electrons by the catalysts. In which process the CO_2 and H^+ were reduced to produce CO and H_2, respectively, at the metal cobalt active sites. Finally, the oxidised $Ru(bpy)_3^{3+}$ was reduced to $Ru(bpy)_3^{2+}$ by TEOA as well as completing the whole cycle (Fig. 7e and f).[76]

Conclusions

This work presents two POMOFs named $Co_2(W_{10}O_{32})(BIA)_4(CH_3CN)_4$ (compound **1**) and $Co_4(W_{10}O_{32})(INA)_6(CH_3CN)_4(TBA)_2$ (compound **2**) with $[W_{10}O_{32}]^{4-}$ clusters as the connecting nodes. Notably, the syngas yield of compound **1** is 42.7 μmol h^{-1} in a flue gas with a 15% CO_2 concentration, which occupies 58% of the syngas yield under pure CO_2 conditions. Furthermore, compound **1** remained active in dilute CO_2 (5–30%) with syngas yields of 23.6–53.3 μmol h^{-1}. Under pure CO_2 conditions, the syngas yield of compound **1** (72.7 μmol h^{-1}) was higher than that of compound **2** (54.2 μmol h^{-1}). Photocurrent tests and Mott–Schottky plots showed that the electron–hole separation and energy level structure of compound **1** were better than those of compound **2**, so that compound **1** was more beneficial for the reduction reaction to give syngas. The density functional theory calculations show that the charge distribution and steric hindrance of compound **1** were also conducive to the reduction reaction. This work provides a suitable catalyst for the preparation of syngas directly from flue gas under photocatalytic conditions.

Conflicts of interest

There are no conflicts to declare.

Acknowledgements

This work was financially supported by the National Natural Science Foundation of China (NSFC) (Grant No. 22271023, and -21971032).

Notes and references

1 R. L. Siegelman, E. J. Kim and J. R. Long, *Nat. Mater.*, 2021, **20**, 1060.
2 J. L. White, M. F. Baruch, J. E. Pander, Y. Hu, I. C. Fortmeyer, J. E. Park, T. Zhang, K. Liao, J. Gu and Y. Yan, *et al.*, *Chem. Rev.*, 2015, **115**, 12888–12935.
3 A. Goeppert, M. Czaun, J. P. Jones, G. K. Surya Prakash and G. A. Olah, *Chem. Soc. Rev.*, 2014, **43**, 7995–8048.

4 M. Mikkelsen, M. Jørgensen and F. C. Krebs, *Energy Environ. Sci.*, 2010, **3**, 43–81.
5 N. S. Lewis and D. G. Nocera, *Proc. Natl. Acad. Sci. U. S. A.*, 2006, **103**, 15729–15735.
6 Z. Y. Sun, T. Ma, H. C. Tao, Q. Fan and B. X. Han, *Chem*, 2017, **3**, 560–587.
7 R. Sahoo, S. Mondal, D. Mukherjee and M. C. Das, *Adv. Funct. Mater.*, 2022, **32**, 2207197.
8 G. V. Last and M. T. Schmick, *Environ Earth Sci.*, 2015, **74**, 1189–1198.
9 X. Y. Wu, Y. Li, G. K. Zhang, H. Chen, J. Li, K. Wang, Y. Pan, Y. Zhao, Y. F. Sun and Y. Xie, *J. Am. Chem. Soc.*, 2019, **141**, 5267–5274.
10 M. Dong, J. Zhou, J. Zhong, H. T. Li, C. Y. Sun, Y. D. Han, J. N. Kou, Z. H. Kang, X. L. Wang and Z. M. Su, *Adv. Funct. Mater.*, 2022, **32**, 2110136.
11 D. Y. Du, J. S. Qin, S. L. Li, Z. M. Su and Y. Q. Lan, *Chem. Soc. Rev.*, 2014, **43**, 4615–4632.
12 J. Liu, Y. Liu, N. Liu, Y. Han, X. Zhang, H. Huang, Y. Lifshitz, S. T. Lee, J. Zhong and Z. Kang, *Science*, 2015, **347**, 970–974.
13 H. J. Yan, C. G. Tian, L. Sun, B. Wang, L. Wang, J. Yin, A. P. Wu and H. G. Fu, *Energy Environ. Sci.*, 2014, **7**, 1939–1949.
14 C. Busche, L. Vila-Nadal, J. Yan, H. N. Miras, D. L. Long, V. P. Georgiev, A. Asenov, R. H. Pedersen, N. Gadegaard, M. M. Mirza, D. J. Paul, J. M. Poblet and L. Cronin, *Nature*, 2014, **515**, 545–549.
15 P. Yang, Y. Xiang, Z. Lin, B. S. Bassil, J. Cao, L. Fan, Y. Fan, M. X. Li, P. Jim8- nez-Lozano, J. J. Carbj, J. M. Poblet and U. Kortz, *Angew. Chem., Int. Ed.*, 2014, **53**, 11974–11978.
16 X. B. Han, Z. M. Zhang, T. Zhang, Y. G. Li, W. Lin, W. You, Z. M. Su and E. B. Wang, *J. Am. Chem. Soc.*, 2014, **136**, 5359–5366.
17 X. Zheng, J. Deng, N. Wang, D. Deng, W. H. Zhang, X. Bao and C. Li, *Angew. Chem., Int. Ed.*, 2014, **53**, 7023–7027.
18 Y. Ding, W. Zhao, W. F. Song, Z. X. Zhang and B. C. Ma, *Green Chem.*, 2011, **13**, 1486–1489.
19 N. Gao, H. J. Sun, K. Dong, J. S. Ren and X. G. Qu, *Chem. – Eur. J.*, 2015, **21**, 829–835.
20 C. M. Granadeiro, P. Silva, V. K. Saini, F. A. A. Paz, J. Pires, L. Cunha-Silva and S. S. Balula, *Catal. Today*, 2013, **218–219**, 35–42.
21 N. Maksimchuk, M. Timofeeva, M. Melgunov, A. Shmakov, Y. Chesalov, D. Dybtsev, V. Fedin and O. Kholdeeva, *J. Catal.*, 2008, **257**, 315–323.
22 J. W. Sun, P. F. Yan, G. H. An, J. Q. Sha, G. M. Li and G. Y. Yang, *Sci. Rep.*, 2016, **6**, 25595.
23 G. Paille, M. Gomez-Mingot, C. Roch-Marchal, B. LassalleKaiser, P. Mialane, M. Fontecave, C. Mellot-Draznieks and A. Dolbecq, *J. Am. Chem. Soc.*, 2018, **140**, 3613–3618.
24 W. Salomon, F. J. Yazigi, C. Roch-Marchal, P. Mialane, P. Horcajada, C. Serre, M. Haouas, F. Taulelle and A. Dolbecq, *Dalton Trans.*, 2014, **43**, 12698–12705.
25 E. V. Ramos-Fernandez, C. Pieters, B. van der Linden, J. JuanAlcañiz, P. Serra-Crespo, M. W. G. M. Verhoeven, H. Niemantsverdriet, J. Gascon and F. Kapteijn, *J. Catal.*, 2012, **289**, 42–52.
26 S. X. L. C. Y. Sun, D. D. Liang, K. Z. Shao, Y. H. Ren and Z. M. Su, *J. Am. Chem. Soc.*, 2009, **131**, 1883–1888.
27 L. Zeng, X. Guo, C. He and C. Duan, *ACS Catal.*, 2016, **6**, 7935–7947.
28 X. T. Zheng, W. L. Chen, L. Chen, Y. J. Wang, X. W. Guo, J. B. Wang and E. B. Wang, *Chem. – Eur. J.*, 2017, **23**, 8871–8878.
29 Y. N. Zhang, Y. Zhang, L. Li, J. L. Chen, P. Z. Li and W. H. Huang, *J. Electroanal. Chem.*, 2020, **861**, 113939.
30 L. Deng, X. Dong and Z. H. Zhou, *Chem. – Eur. J.*, 2021, **27**, 9643–9653.
31 W. A. Shah, A. Waseem, M. A. Nadeem and P. Kögerler, *Appl. Catal., A*, 2018, **567**, 132–138.
32 Q. Lan, Z. M. Zhang, C. Qin, X. L. Wang, Y. W. Li, H. Q. Tan and E. B. Wang, *Chem. – Eur. J.*, 2016, **22**, 15513–15520.
33 Y. N. Liu, J. Wang, K. H. Ji, S. Meng, Y. H. Luo, H. F. Li, P. T. Ma, J. Y. Niu and J. P. Wang, *J. Catal.*, 2022, **416**, 149–156.
34 X. M. Wang, Z. M. Feng, B. X. Xiao, J. X. Zhao, H. Y. Ma, Y. Tian, H. J. Pang and L. C. Tan, *Green Chem.*, 2020, **22**, 6157–6169.
35 S. M. Liu, Z. Zhang, X. Li, H. Jia, M. Ren and S. Liu, *Adv. Mater. Interfaces*, 2018, **5**, 1801062.
36 X. X. Li, J. Liu, L. Zhang, L. Z. Dong, Z. F. Xin, S. L. Li, X. Q. Huang-Fu, K. Huang and Y. Q. Lan, *ACS Appl. Mater. Interfaces*, 2019, **11**, 25790–25795.
37 J. Du, Y. Y. Ma, W. J. Cui, S. M. Zhang, Z. G. Han, R. H. Li, X. Q. Han, W. Guan, Y. H. Wang, Y. Q. Li, Y. Liu, F. Y. Yu, K. Q. Wei, H. Q. Tan, Z. H. Kang and Y. G. Li, *Appl. Catal., B*, 2022, **318**, 121812.
38 W. F. Wu, Z. H. Fu, S. B. Tang, S. Zou, X. Wen, Y. Meng, S. B. Sun, J. Deng, Y. C. Liu and D. L. Yin, *Appl. Catal., B*, 2015, **164**, 113–119.
39 M. Filowitz, R. K. C. Ho, W. G. Klemperer and W. Shum, *Inorg. Chem.*, 1979, **18**, 1.
40 Y. T. Zhang, X. L. Wang, S. B. Li, Y. R. Gong, B. Q. Song, K. Z. Shao and Z. M. Su, *Chem. Commun.*, 2016, **52**, 9632–9635.
41 D. Y. Shi, J. W. Zhao, L. J. Chen, P. T. Ma, J. P. Wang and J. J. Niu, *CrystEngComm*, 2012, **14**, 3108–3119.
42 J. W. Zhao, D. Y. Shi, L. J. Chen, X. M. Cai, Z. Q. Wang, P. T. Ma, J. P. Wang and J. Y. Niu, *CrystEngComm*, 2012, **14**, 2797–2806.
43 D. Y. Shi, Z. Ming, Q. Y. Wu, T. H. Lai, K. J. Zheng, C. He and J. W. Zhao, *Inorg. Chem. Commun.*, 2019, **100**, 125–128.
44 D. Y. Shi, R. Zheng, M. J. Sun, X. R. Cao, C. X. Sun, C. J. Cui, C. S. Liu, J. W. Zhao and M. Du, *Angew. Chem., Int. Ed.*, 2017, **56**, 14637–14641.
45 W. Yan, L. J. Han, H. L. Jia, K. Shen, T. Wang and H. G. Zheng, *Inorg. Chem.*, 2016, **55**, 8816–8821.
46 D. Y. Shi, L. Zeng, Z. Ming, C. He, C. G. Meng and C. Y. Duan, *RSC Adv.*, 2016, **6**, 51936–51940.
47 R. M. Irfan, T. T. Wang, D. C. Jiang, Q. D. Yue, L. Zhang, H. Y. Cao, Y. Pan and P. W. Du, *Angew. Chem., Int. Ed.*, 2020, **59**, 14818–14824.

48 M. Dong, J. Zhou, J. Zhong, H. T. Li, C. Y. Sun, Y. D. Han, J. N. Kou, Z. H. Kang, X. L. Wang and Z. M. Su, *Adv. Funct. Mater.*, 2022, **32**, 2110136.
49 J. J. Su, D. Wang, Y. D. Wang, H. B. Zhou, C. Liu, S. Liu, C. M. Wang, W. M. Yang, Z. K. Xie and M. Y. He, *ChemCatChem*, 2018, **10**, 1536–1541.
50 Y. M. Ni, Y. Liu, Z. Y. Chen, M. Yang, H. C. Liu, Y. L. He, Y. Fu, W. L. Zhu and Z. M. Liu, *ACS Catal.*, 2019, **9**, 1026–1032.
51 A. V. Kirilin, J. F. Dewilde, V. Santos, A. Chojecki, K. Scieranka and A. Malek, *Ind. Eng. Chem. Res.*, 2017, **56**, 13392–13401.
52 S. H. Guo, Xi. J. Qi, H. M. Zhou, J. Zhou, X. H. Wang, M. Dong, X. Zhao, C. Y. Sun, X. L. Wang and Z. M. Su, *J. Mater. Chem. A*, 2020, **8**, 11712–11718.
53 A. Zhou, Y. B. Dou, C. Zhao, J. Zhou, X. Q. Wu and J. R. Li, *Appl. Catal., B*, 2020, **264**, 118519.
54 Y. Li, B. H. Li, D. N. Zhang, L. Cheng and Q. J. Xiang, *ACS Nano*, 2020, **14**, 10552–10561.
55 L. J. Liu, Y. Q. Jiang, H. L. Zhao, J. T. Chen, J. L. Cheng, K. S. Yang and Y. Li, *ACS Catal.*, 2016, **6**, 1097–1108.
56 T. Tian, X. Y. Jin, N. Guo, H. Q. Li, Y. Han and Y. P. Yuan, *Appl. Catal., B*, 2022, **308**, 121227.
57 F. Guo, R. X. Li, S. Z. Yang, X. Y. Zhang, H. J. Yu, J. J. Urban and W. Y. Sun, *Angew. Chem., Int. Ed.*, 2023, **62**, e202216232.
58 T. T. Yan, P. Wang and W. Y. Sun, *Small*, 2023, **19**, 2206070.
59 Y. Zhang, X. Y. Zhang and W. Y. Sun, *ACS Catal.*, 2023, **13**, 1545–1553.
60 S. Saha, G. Das, J. Thote and R. Banerjee, *J. Am. Chem. Soc.*, 2014, **136**, 14845–14851.
61 K. F. Li, X. Q. An, K. H. Park, M. Khraisheh and J. W. Tang, *Catal. Today*, 2014, **224**, 3–12.
62 Y. Xie, Z. B. Fang, L. Li, H. X. Yang and T. F. Liu, *ACS Appl. Mater. Interfaces*, 2019, **11**, 27017–27023.
63 K. B. Zhong, C. H. Shan, L. Zhu, S. Liu, T. Zhang, F. R. Liu, B. M. Shen, Y. Lan and R. P. Bai, *J. Am. Chem. Soc.*, 2019, **141**, 5772–5780.
64 T. Lu and Q. X. Chen, *Chem.: Methods*, 2021, **1**, 231–239.
65 X. B. Han, C. Qin, X. L. Wang, Y. Z. Tan, X. J. Zhao and E. B. Wang, *Appl. Catal., B*, 2017, **211**, 349–356.
66 X. Y. Dao and W. Y. Sun, *Inorg. Chem. Front.*, 2021, **8**, 3178–3204.
67 X. Y. Dao, J. H. Guo, Y. P. Wei, F. Guo, Y. Liu and W. Y. Sun, *Inorg. Chem.*, 2019, **58**, 8517–8524.
68 Y. Ghandour, C. Mchiri, I. Mestiri, A. Y. A. Alzahrani and H. Nasri, *J. Chem. Sci.*, 2022, **134**, 78.
69 D. F. Pereira, E. R. Santana, J. V. Piovesan and A. Spinelli, *Diamond Relat. Mater.*, 2020, **105**, 107793.
70 M. Guergueb, F. Loiseau, F. Molton, H. Nasri and A. Klein, *Molecules*, 2022, **27**, 1705.
71 Z. Li, J. D. Xiao and H. L. Jiang, *ACS Catal.*, 2016, **6**, 5359–5365.
72 K. Zhao, S. L. Zhao, C. Gao, J. Qi, H. J. Yin, D. Wei, M. F. Mideksa, X. L. Wang, Y. Gao, Z. Y. Tang and R. B. Yu, *Small*, 2018, **14**, 1800762.
73 C. Creutz and N. Sutin, *Inorg. Chem.*, 1976, **15**, 496–499.
74 M. Lu, M. Zhang, J. Liu, T. Y. Yu, J. N. Chang, L. J. Shang, S. L. Li and Y. Q. Lan, *J. Am. Chem. Soc.*, 2022, **144**, 1861–1871.
75 L. Hao, R. C. Shen, C. Huang, Z. Z. Liang, N. Li, P. Zhang, X. Z. Li, C. C. Qin and X. Li, *Appl. Catal., B*, 2023, **330**, 122581.
76 B. Probst, A. Rodenberg, M. Guttentag, P. Hamm and R. Alberto, *Inorg. Chem.*, 2010, **49**, 6453–6460.

